

Article

# Enhancing CO<sub>2</sub> Adsorption on MgO: Insights into Dopant Selection and Mechanistic Pathways

Shunnian Wu<sup>1</sup>, W. P. Cathie Lee<sup>1</sup> , Hashan N. Thenuwara<sup>1</sup> , Xu Li<sup>2,\*</sup> and Ping Wu<sup>1,\*</sup> 

<sup>1</sup> Entropic Interface Group, Engineering Product Development, Singapore University of Technology and Design, 8 Somapah Road, Singapore 487372, Singapore

<sup>2</sup> Institute of Materials Research and Engineering, Agency for Science, Technology and Research (A\*STAR), Fusionopolis Way, Innovis, Singapore 138634, Singapore

\* Correspondence: x-li@imre.a-star.edu.sg (X.L.); wuping@sutd.edu.sg (P.W.)

**Abstract:** Inspired by our recent success in designing CO<sub>2</sub>-phobic and CO<sub>2</sub>-philic domains on nano-MgO for effective CO<sub>2</sub> adsorption, our ongoing efforts focus on incorporating dopants into pristine MgO to further enhance its CO<sub>2</sub> adsorption capabilities. However, a clear set of guidelines for dopant selection and a holistic understanding of the underlying mechanisms is still lacking. In our investigation, we combined first-principles calculations with experimental approaches to explore the crystal and electronic structural changes in MgO doped with high-valence elements (Al, C, Si, and Ti) and their interactions with CO<sub>2</sub>. Our findings unveiled two distinct mechanisms for CO<sub>2</sub> capture: Ti-driven catalytic CO<sub>2</sub> decomposition and CO<sub>2</sub> polarization induced by Al, C, and Si. Ti doping induced outward Ti atom displacement and structural distortion, facilitating CO<sub>2</sub> dissociation, whereas C doping substantially bolstered the electron donation capacity and CO<sub>2</sub> adsorption energy. Pristine and C-doped MgO engaged CO<sub>2</sub> through surface O atoms, while Al-, Si-, and Ti-doped MgO predominantly relied on dopant–O atom interactions. Our comprehensive research, integrating computational modeling and experimental work supported by scanning electron microscopy and thermal gravimetric analysis, confirmed the superior CO<sub>2</sub> adsorption capabilities of C-doped MgO. This yielded profound insights into the mechanisms and principles that govern dopant selection and design.

**Keywords:** MgO; CO<sub>2</sub> adsorption; doping; charge donation; uneven electron distribution



Academic Editor: Hermann Ehrlich

Received: 27 November 2024

Revised: 24 December 2024

Accepted: 25 December 2024

Published: 27 December 2024

**Citation:** Wu, S.; Lee, W.P.C.; Thenuwara, H.N.; Li, X.; Wu, P. Enhancing CO<sub>2</sub> Adsorption on MgO: Insights into Dopant Selection and Mechanistic Pathways. *Biomimetics* **2025**, *10*, 9. <https://doi.org/10.3390/biomimetics10010009>

**Copyright:** © 2024 by the authors. Licensee MDPI, Basel, Switzerland. This article is an open access article distributed under the terms and conditions of the Creative Commons Attribution (CC BY) license (<https://creativecommons.org/licenses/by/4.0/>).

## 1. Introduction

The rise in greenhouse gas emissions has greatly accelerated global climate change. Among these emissions, carbon dioxide (CO<sub>2</sub>), primarily generated from fossil fuel combustion, constitutes approximately 70% of the total greenhouse gases released into the atmosphere [1]. Flue gases, which are released during industrial and power generation processes, are a major source of CO<sub>2</sub>. The efficient capture of CO<sub>2</sub> from flue gases offers a promising strategy for mitigating the rise in greenhouse gas emissions. Among the various approaches, carbon capture and storage (CCS) technology stands out as an effective solution to address the challenges of climate change. CCS encompasses an integrated process involving CO<sub>2</sub> capture, transportation, storage, and utilization. CO<sub>2</sub> capture methods can be broadly categorized into adsorption, absorption, membrane separation, and cryogenic distillation techniques [2]. Among these, adsorption has been regarded as a competitive solution owing to its simple process, mild operating conditions, large operating flexibility, wide operating temperature range, lack of corrosion and fouling, stable performance, and low operating cost [2].

MgO has attracted extensive attention to be employed as a solid CO<sub>2</sub> adsorbent to reduce CO<sub>2</sub> due to its rich sources and low cost as well as its high theoretical CO<sub>2</sub> adsorption capacity [3]. It is well known that pristine MgO exhibits a relatively low CO<sub>2</sub> adsorption capacity, with commercial MgO adsorbing only 1.9 mg/g at 200 °C [4] and another study reporting 8.8 mg/g at 50 °C [5]. The limited adsorption capacity of unmodified MgO is one of the main reasons why structural modification and doping have attracted continuous research interest as a method to improve MgO's performance. Inspired by the interwoven or intermittent water harvesting mechanism of the Namib desert beetles [6], which features alternating regions—a water capture region with high water adsorption and a water transport region with low water adsorption—our research group innovatively developed interwoven CO<sub>2</sub>-phobic and CO<sub>2</sub>-philic domains on electrospun nano-MgO, leading to a significant improvement in CO<sub>2</sub> adsorption as high as 41 mg/g [7]. Another example of structural modification was demonstrated when Sun et al. decomposed Mg(OH)<sub>2</sub> to produce MgO with a CO<sub>2</sub> adsorption performance of 33 mg/g [8]. Additionally, many dopants have been introduced to MgO using different synthesis approaches. MgO containing 15 wt% La<sub>2</sub>O<sub>3</sub> shows a comparatively high CO<sub>2</sub> capacity of 26 mg/g and excellent cyclic stability [9]. The formatted carbonate layers were claimed not to shelter the abundant pores in the inside or outside of the hollow microspheres due to the increased oxygen vacancy with the addition of La [9]. Cs-doped MgO reports a CO<sub>2</sub> sorption capacity of 76.6 mg/g at an adsorption temperature of 300 °C and 32.2 mg/g at 235 °C. It is speculated that the Cs doping should be increased so that a greater portion of adsorbent can react with CO<sub>2</sub> to form a mixed Mg–Cs carbonate phase at a lower activation energy [10]. MgO that was introduced with elemental Fe and Ni by a ball-milling process obtained CO<sub>2</sub> adsorption capacities of 36.3 and 60.9 mg/g, respectively [11]. This is significantly higher compared with the CO<sub>2</sub> adsorption capacity of 15.7 mg/g for the undoped MgO synthesized by a solution–combustion process. Ni doping shows a more favorable influence on CO<sub>2</sub> adsorption than Fe doping, since it brings about a narrower particle size distribution, which generates more active sites for CO<sub>2</sub> adsorption. The incorporation of Al is claimed to fully expose the alkaline binding sites on the MgO surface, thereby promoting the adsorption capacity of CO<sub>2</sub> and achieving an enhanced CO<sub>2</sub> adsorption capacity of 34.1 mg/g [12]. This significant improvement in CO<sub>2</sub> adsorption can be attributed to the excellent dispersity of MgO particles and the shortened diffusion path for CO<sub>2</sub> molecules. A synergistic interaction between co-doped Al and C has been shown to produce highly unsaturated basic O<sup>2−</sup> sites, enhancing CO<sub>2</sub> adsorption [13]. Al-C-doped MgO instantly adsorbs 34.6 mg/g CO<sub>2</sub> in the harsh environment of 200 °C. MgO doped with Cu [14], Zn [4], and Zr [15,16] achieved high sorption capacity of 34.6 mg/g [14], 33.3 mg/g [4], and 51.6 mg/g [15], respectively. It is proposed that the metal incorporation increases the surface defects of magnesia nanoparticles and generates abundant basic sites.

CO<sub>2</sub> adsorption can be accomplished by dispersion forces or by carbonate formation via reaction with the five-coordinated O<sup>2−</sup> ion on the exposed MgO surface. A theoretical study uncovered that no carboxylate species can form on the (100) surface of MgO in the absence of point defects [17]. On the other hand, doping with alkaline metals (Li, Na, K, and Rb) brings about a large increase in CO<sub>2</sub> adsorption energies [18]. Therefore, all alkali metals enhance CO<sub>2</sub> adsorption. Additionally, Sr doping on this enhanced surface makes the system more effective as a reversible CO<sub>2</sub> adsorbent by lowering the adsorption energy of CO<sub>2</sub> [19]. When doped with Al or any metal that is capable of acting as an electron donor, the formation of carboxylate species (CO<sub>2</sub><sup>−</sup>) is favored. This is because the CO<sub>2</sub> in the physisorbed state is unstable and will spontaneously transform into the carboxylate complex in the presence of an excess electron [17]. Although the doping of the MgO surface with Ni is found to have a weak effect on the energies of CO<sub>2</sub> chemisorption [20], the

introduction of intermetallics, NiM (M = Mn, Fe, Co, and Cu), on the MgO surface shows a stronger adsorption of CO<sub>2</sub>, which depends on the binding energies of NiM on MgO [20]. In the case of monometallic doping, the average CO<sub>2</sub> adsorption energies of doped MgO increase in the order of Ca, Fe, and Al doping corresponding to the relevant chemical valence (+2 for Ca, +2/+3 for Fe, and +3 for Al) [21]. Strong attractive forces of CO<sub>2</sub> to dopant atoms are mostly responsible for the increased adsorption strengths, especially for Al atoms. The CO<sub>2</sub> binding interaction with the basic O sites in the doped MgO surface is enhanced compared with the undoped MgO surface. It is suggested that Al-doped MgO is more suitable as a CO<sub>2</sub> adsorbent than Ca/Fe-doped MgO [22].

Despite ongoing experimental and theoretical research on doping strategies to enhance CO<sub>2</sub> adsorption, clear guidelines for dopant selection and the underlying improvement mechanisms remain lacking. In the present study, CO<sub>2</sub> adsorption on a pristine MgO (100) surface and a MgO (100) surface doped with selected dopants was evaluated. Density of states (DOS) and density-derived electrostatic chemical (DDEC) analyses [23–26] were conducted to characterize the doping effects and exploit the mechanism.

## 2. Materials and Methods

### 2.1. Theoretical Simulation of CO<sub>2</sub> Adsorption

The Vienna ab initio simulation package (VASP) [27] was employed to carry out the first-principles calculations with the Perdew–Burke–Ernzerhof (PBE) generalized gradient approximation (GGA) exchange–correlation functional [28]. A projector augmented wave (PAW) method [29,30] was applied as a plane-wave basis set to describe the electron–core interaction. A kinetic energy cutoff of 500 eV was applied for the plane-wave expansion. The van der Waals interactions were accounted for using the DFT+D3 correction method [31]. The total energy convergence was set as  $1.0 \times 10^{-6}$  eV, and the forces on each individual atom were minimized to be smaller than 0.01 eV/Å for geometry optimization and total energy calculations. The value for smearing was fixed at 0.01 eV. A Monkhorst–Pack [32] K-points mesh was adopted for sampling the Brillouin zone, and the K-points number (NK) was adjusted to keep  $NK \times L$  (L is the lattice constant) being about 25 Å for structural relaxations and 45 Å for electronic calculations, respectively.

The MgO crystalline structure obtained in a previous study [33] is used in this work. Its crystalline structure was cleaved in the most stable (001) direction [34] to investigate its ability to achieve CO<sub>2</sub> adsorption. The MgO slabs were composed of six layers from the  $3 \times 3$  expansion of the MgO unit cell. The lowest 3 layers remained fixed in their bulk locations while the top 3 layers and CO<sub>2</sub> molecule were free to move. The doping effect on adsorption behavior was investigated by substituting one Mg atom with a dopant atom on the MgO (100) subsurface. One CO<sub>2</sub> molecule was placed next to the dopant to evaluate its effect. To ensure that the interaction force between the layer planes was minimal, a 20 Å vacuum thickness was maintained between them. The CO<sub>2</sub> adsorption energy  $E_{ad}$  is defined as  $E_{ad} = E_{surface+CO_2} - E_{CO_2} - E_{surface}$ , where  $E_{surface+CO_2}$  is the total energy of the system with the CO<sub>2</sub> molecule,  $E_{CO_2}$  is the energy of the CO<sub>2</sub> molecule, and  $E_{surface}$  is the total energy of the system. A lower value for  $E_{ad}$  indicates a stronger adsorption of CO<sub>2</sub> on the surface. The DDEC6 analysis was calculated using the Chargemol package [35]. The simulation procedure [36] is outlined in Table S1.

### 2.2. Materials

Magnesium acetate tetrahydrate (Mg(CH<sub>3</sub>COO)<sub>2</sub>·4H<sub>2</sub>O) (ACS reagent, ≥98%) and poly(vinyl alcohol) (Mw 30,000–50,000, 87–90% hydrolyzed) were purchased from Sigma Aldrich (Merck Pte. Ltd., Singapore). Deionized water was obtained from Neptec Halios lab water system.

### 2.3. Preparation of MgO and C-Doped MgO Nanoparticles

MgO nanoparticles and C-doped MgO nanoparticles were synthesized using the spray-drying method. Initially, 4 g of magnesium acetate tetrahydrate were dissolved in deionized water to prepare a 40 g/L precursor solution. For the synthesis of C-doped MgO, additional polyvinyl alcohol was introduced into the solution at a 1:10 molar ratio to magnesium acetate tetrahydrate. This solution was fed into a laboratory scale mini spray dryer machine (BUCHI Mini Spray Dryer B-290, BUCHI, Flawil, Switzerland) at a flow rate of 10 mL/min and an evaporation temperature of 220 °C. The powder collected from the spray dryer was calcined in a muffle furnace (Carbolite ELF, Carbolite Gero, Derbyshire, UK) at 350 °C for 1 h, with a ramping rate of 2 °C/min. After natural cooling to room temperature, the calcined material was ground into fine nanopowder using a mortar and pestle, yielding the final nanoparticles.

### 2.4. Morphology Characterization and CO<sub>2</sub> Adsorption Measurement

Surface morphology was characterized using FESEM instrument (JEOL JSM-7600F, Jeol, Tokyo, Japan). X-ray diffraction (XRD) analysis was performed using a Bruker D8 Advance X-ray diffractometer (Bruker, Karlsruhe, Germany) with Cu-K $\alpha$  radiation ( $\lambda = 1.54 \text{ \AA}$ ), operating at 40 kV and 25 mA. CHNS analysis was conducted using a Thermo Scientific Flash EA 1112 Series CHNS-O analyzer (Thermo Scientific, Waltham, MA, USA) to determine the carbon content of the doped sample. CO<sub>2</sub> capture capacity was measured by thermogravimetric analysis (TGA) using TGA Q50 analyzer (TA Instruments, New Castle, DE, USA). For TGA, initially, samples were preheated at 150 °C for 60 min under high-purity N<sub>2</sub> gas flow (40 mL/min) to remove preabsorbed moisture and other contaminants from the atmosphere during storage. Subsequently, high-purity CO<sub>2</sub> gas was introduced at 30 °C at a rate of 40 mL/min for designated time period. The CO<sub>2</sub> capture capacity was calculated from the weight gain of the sample during CO<sub>2</sub> gas feed.

## 3. Results and Discussion

### 3.1. Structure of Pristine and Doped MgO Surface

We replaced one Mg atom with one dopant atom, i.e., Al, C, Si, or Ti on the MgO surface in this work. Figure 1 shows the optimized structures of the doped MgO surfaces in comparison with the pristine MgO surface. The Mg atoms on the surface are five-coordinated with four equivalent surface O atoms to form Mg-O bonds of 2.13 Å and one slightly shorter vertical Mg-O bond of 2.09 Å. Al doping generates shorter Al-O bonds, indicating stronger interaction. The doped C shifts deeper to the layer next to the surface, with a significantly shorter C-O bond of 1.27 Å, which is close to the C=O bond of 1.28 Å in a carbonate group [37]. Contrarily, the C-O bond with the four surface O atoms is weak, and the bond length is 2.34 Å. Therefore, the C atom deviates from the original lattice site, and a defect is generated. Doped Si seems to move slightly inward to the neighboring layer, which may slightly stretch the four equivalent surface Si-O bonds. The dopant Ti shows exceptional outward movement, and the bond length of Ti with the O in the neighboring layer increases by 0.09 Å. Moreover, its bonds with the four surface O atoms are not equivalent, indicating torture of the structure. This may be attributed to the bonding using 3d orbitals of the transition metal atoms.

Table 1 lists the calculated doping energy  $E_f$  required to dope the atom in the substitutional site using the following equation:

$$E_f = E_{MgO-X} - E_{MgO} + E_{Mg} - E_X \quad (1)$$

where  $E_{MgO}$  and  $E_{MgO-X}$  are the energy of the parent MgO surface and doped MgO surface, respectively;  $E_{Mg}$  and  $E_X$  are the calculated energies of the element Mg and dopants, respectively, in their most stable structure [38], i.e., Mg of hexagonal  $P6_3/mmc$  space group, Si of diamond  $Fd\bar{3}m1$ , C of hexagonal  $P6_3/mmc$  structure, Al of hexagonal  $P6_3/mmc$  structure, Ti of hexagonal close-packed  $P6_3/mmc$ . It is observed that the  $E_f$  for Al doping is the smallest, while the  $E_f$  for C doping is the largest. A larger  $E_f$  value indicates more energy input is required to generate the dopant site in the structure; therefore, it is tougher to obtain the doped structure. This may explain the abundance of experiments on Al-doped MgO and the lack of experiments on the other doped MgO surfaces.

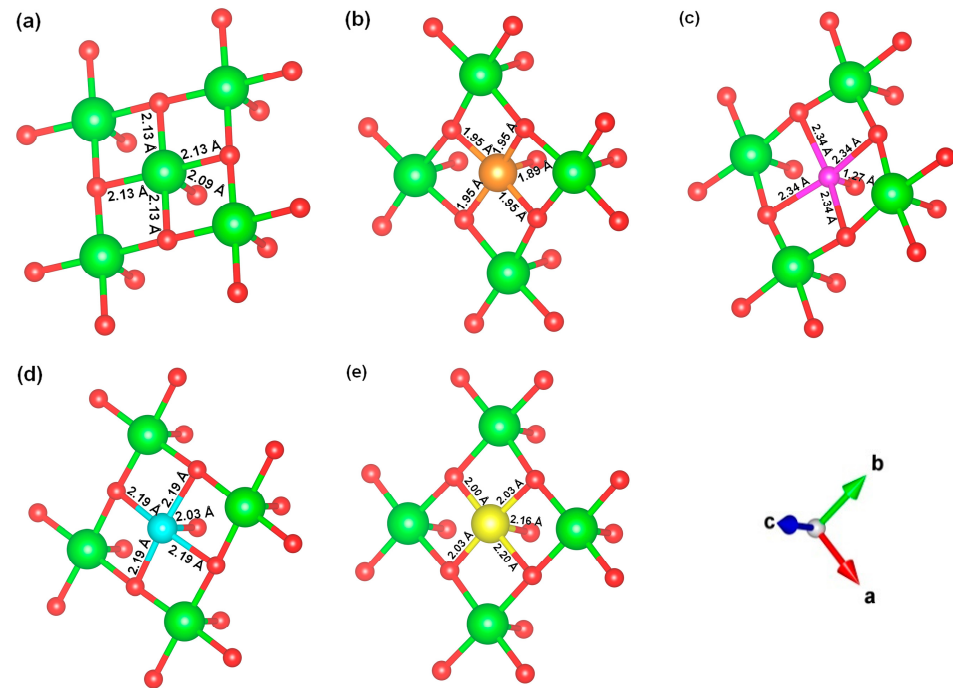


**Figure 1.** Optimized structure of MgO surface (a) and MgO surface doped with Al (b), C (c), Si (d), and Ti (e). Red, green, coral, magenta, cyan, and yellow balls represent O, Mg, Al, C, Si, and Ti atoms, respectively.

**Table 1.** Doping formation energy and charge transfer capacity of various dopants in doped MgO.

Dopant	$E_f$ , eV	Charge Transfer Capacity
- *		0.54
Al	1.24	1.30
C	9.07	3.70
Si	3.64	3.37
Ti	2.04	2.54

\* "-" indicates the absence of a dopant in pristine MgO. This notation is consistently applied in the subsequent Tables.

The charge donation capacity is obtained by deduction of the calculated net atomic charge with the DDEC6 analysis from its valence electrons. It is observed that each Mg donates 0.54 electrons in pristine MgO, which is the least compared with all the dopants studied. Al donates more than double the electrons to MgO surfaces compared with Mg. However, less than half of its three valence electrons take part in direct bonding with neighboring O atoms. A significant increase in charge donation capacity is observed in C and Si, which donate 3.70 and 3.37 electrons to the structure, respectively. This implies that nearly all their four valence electrons are involved in bonding, which suggests about a 3.7+ and 3.4+ nominal valence state for C and Si, respectively. Ti shows about a 2.5+ nominal

valence state, giving much larger charge transfer capacity than Mg. Niedermaier et al. also reported that while Co substitutes the host ions in the cationic sublattice of MgO,  $\text{Co}^{2+}$  ions keep their divalent valence state [39]. The increased electron transfer capacity of the dopant in doped MgO can transfer more electrons to the introduced  $\text{CO}_2$  molecules, thus improving its  $\text{CO}_2$  adsorption behavior [33].

### 3.2. Simulated $\text{CO}_2$ Adsorption on Pristine and Doped MgO

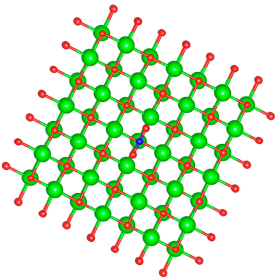
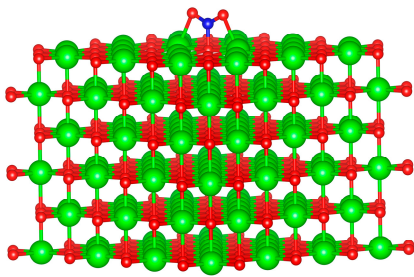
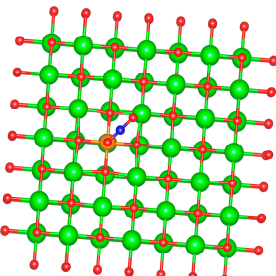
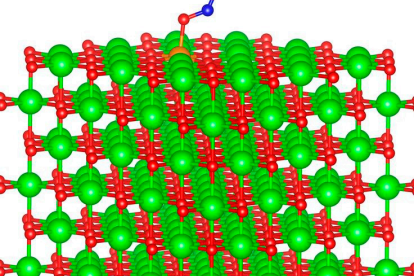
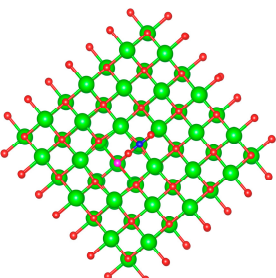
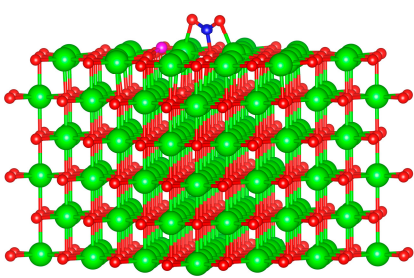
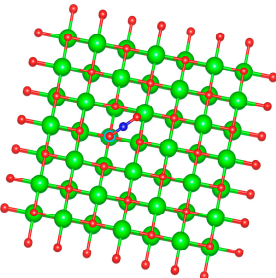
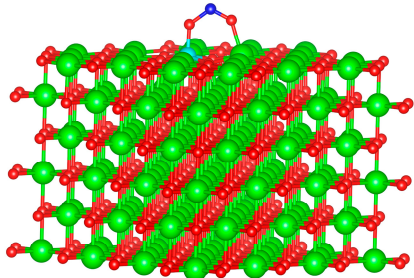
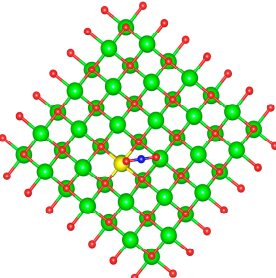
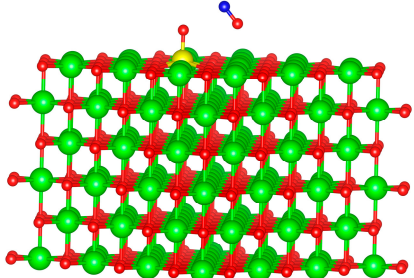
Typical adsorption sites [17,40,41], i.e., the on-top site of O, on-top site of the dopant, bridging site of the Mg-O bond, bridging site of the dopant-O bond, and hole site, as shown in Figure S1, have been evaluated in our preliminary work.  $\text{CO}_2$  energetically prefers to adsorb on the on-top site of O on both pristine and C-doped MgO surfaces. Kim et al. [42] also reported that  $\text{CO}_2$  is strongly adsorbed at the on-top site of the oxygen on the MgO (100) surface.  $\text{CO}_2$  energetically prefers the hole site on Al-, Si-, and Ti-doped MgO surfaces. This is consistent with Lv et al.'s report that  $\text{CO}_2$  is strongly adsorbed at the hole sites on the Al-doped MgO (100) surface [43]. Table 2 summarizes the initial and optimized configurations for MgO with the adsorbate molecule  $\text{CO}_2$ . The adsorbed  $\text{CO}_2$  molecule has changed from a linear shape to a bent structure in the pristine MgO and MgO doped with Al, C, and Si. Direct bonding of the O of the  $\text{CO}_2$  molecule with the dopant is observed in Al-, Si-, and Ti-doped MgO. The bonding stabilizes the adsorbed  $\text{CO}_2$  molecules, which explains the fact that  $\text{CO}_2$  prefers hollow sites in these MgO surfaces. However, due to the small size of the C cation, the bonding of O of  $\text{CO}_2$  with the dopant C does not occur; therefore,  $\text{CO}_2$  prefers the on-top site of O on the C-doped MgO surface.

Table 3 lists the calculated  $\text{CO}_2$  adsorption energies for pristine and doped MgO surfaces. All dopants negatively increase the  $\text{CO}_2$  adsorption energy. This indicates enhanced  $\text{CO}_2$  adsorption. Al doping negatively increases the adsorption energy by 37.5%, which is consistent with the significantly improved  $\text{CO}_2$  adsorption observed in experiments [12]. C, Si, and Ti doping dramatically increases the adsorption energy, indicating significantly enhanced affinity for  $\text{CO}_2$  molecules. This implies that MgO doped with C, Si, and Ti should exhibit noticeably improved  $\text{CO}_2$  adsorption performance. The distances of  $\text{CO}_2$  molecules from the surfaces and their structural parameters are listed in Table 3. The distances between  $\text{CO}_2$  and the surface ranged from 1.42 Å to 1.83 Å. C atoms of the adsorbed  $\text{CO}_2$  molecules are nearer to the pristine and C-doped MgO surfaces, whereas O atoms of the adsorbed  $\text{CO}_2$  molecules are nearer to the Al-, Si-, and Ti-doped MgO surfaces. It is noticed that the distance between  $\text{CO}_2$  and the surface is generally smaller for  $\text{CO}_2$  adsorption at the on-top site with an O preference.

The adsorption of  $\text{CO}_2$  can be described as a two-step process [44]: First,  $\text{CO}_2$  undergoes a deformation from its linear gas phase structure into a bent  $\text{CO}_2$  fragment; the deformation may be caused by the coordination of one carbon dioxide oxygen atom to the metal center. Second, the bent  $\text{CO}_2$  fragment binds to the substrate, which drives the adsorption process and reflects the adsorption capability of the substrate. Our calculated O-C-O bond angle ( $\angle\text{OCO}$ ) of  $\text{CO}_2$  ranged from  $116.37^\circ$  to  $134.00^\circ$ , and the C-O bond length ( $d_{\text{C-O}}$ ) ranged from 1.24 Å to 1.42 Å, which are dramatically different from those of free  $\text{CO}_2$  molecules. The C=O bond length in carbon dioxide is 1.16 Å [37]. In its normal state, the C-O bond length is just 1.43 Å; however, the bond length can be stretched to 1.54 Å [37]. Therefore, the bond length shown in Table 3 indicates that the bonding in  $\text{CO}_2$  has not changed to a single C-O bond. Bond lengths of C=O bonds are around 1.23 Å in carbonyl groups and 1.28 Å in carbonate group anions [37]. Therefore,  $\text{CO}_2$  adsorption on the doped MgO surface may be due to chemisorption through the formation of a carbonate structure. The Ti-doped MgO surface shows the strongest polarization toward the  $\text{CO}_2$  molecule, eventually breaking its O=C=O structure, which may be attributed to the 3d orbitals of the Ti dopant. This suggests

an additional benefit of the CO<sub>2</sub> reduction reaction. This validates the effectiveness of using charge transfer to overcome the CO<sub>2</sub> activation barrier during the initial stage of the CO<sub>2</sub> reduction reaction, as indicated in Table 2. In the case of MOF-based nanomaterials, CO<sub>2</sub> has been reduced by Ni, Co, Zn, and Cu using this strategy [45].

**Table 2.** Initial and optimized configuration of CO<sub>2</sub> adsorption on MgO and MgO doped with Al, C, Si, and Ti.

Dopant	Initial Configuration	Most Stable Structure
-		
Al		
C		
Si		
Ti		

**Table 3.** Adsorption energy and structural parameters of adsorbed CO<sub>2</sub> molecule.

Dopant	E <sub>ad</sub>	Distance, Å	CO <sub>2</sub> Molecule		
			<OCO, deg	d <sub>C-O</sub> *, Å	d <sub>C-O</sub> *, Å
-	-0.72	1.44	132.61	1.26	1.26
Al	-0.99	1.83	134.00	1.24	1.26
C	-2.77	1.42	129.35	1.26	1.27
Si	-1.39	1.63	116.37	1.27	1.42
Ti	-2.80	n/a	n/a	n/a	n/a

\* d<sub>C-O</sub> denotes C-O bond length.

### 3.3. Density of States and Charge Transfer Analysis

The density of states (DOS) analysis [33] was carried out and is shown in Figure 2 to reveal the interaction of the CO<sub>2</sub> molecule with pristine and doped MgO (100) surfaces. In order to achieve clear observation, the projected density of states (PDOS) of the dopant is magnified 25-fold; the PDOS of C and O of CO<sub>2</sub> are magnified 25-fold for pristine MgO as well as Al- and C-doped MgO and magnified 5-fold for Si- and Ti-doped MgO. For the pristine MgO surface, the DOS shows weak interactions between CO<sub>2</sub> and the surface atoms. There is a slight overlapping of the minor C peak from CO<sub>2</sub> with the O peak from MgO at -3.4 eV, suggesting minimal bonding contributions. An additional overlap occurs at -1.6 eV between the O peak of CO<sub>2</sub> and the Mg peak of the surface, confirming weak physisorption of CO<sub>2</sub> with no significant orbital hybridization. The minimal interaction aligns with the low CO<sub>2</sub> adsorption energy observed for pristine MgO. Doping with Al leads to noticeable changes in the electronic states. A distinct Al peak appears at -6.8 eV, which strongly overlaps with the major O peak of CO<sub>2</sub>. This overlap indicates strong orbital interactions and hybridization between the Al dopant and O atom of CO<sub>2</sub>. Additionally, an overlap between the O peak of CO<sub>2</sub> and the Mg peak at -3.9 eV further enhances the interaction. The improved adsorption energy in the Al-doped MgO can thus be attributed to the strong Al-O hybridization due to the overlap at -6.8 eV. C doping introduces a unique electronic signature in the DOS. A sharp peak at 2.5 eV overlaps with a minor O peak of CO<sub>2</sub>, indicating significant interaction between the C dopant and the CO<sub>2</sub> molecule. Overlaps occur at multiple lower-energy positions, i.e., -5.8 eV between the C dopant and O (MgO), -4.8 eV of the minor C peak of CO<sub>2</sub> overlapping with the surface O peak, -2.4 eV of the O peak of CO<sub>2</sub> interacting with the Mg peak. The multiple overlaps demonstrate that C doping enhances the interaction between the C of CO<sub>2</sub> and O of the MgO surface and the O of CO<sub>2</sub> and Mg of the surface. Significant changes are observed in the DOS of Si-doped MgO. A dominant Si peak appears at -7.6 eV, strongly overlapping with the major O peak of CO<sub>2</sub>. This strong hybridization suggests a robust Si-O interaction, which significantly enhances CO<sub>2</sub> adsorption. An additional interaction occurs at -5.7 eV, where the minor O peak of CO<sub>2</sub> overlaps with the surface Mg peak. The Si-O orbital hybridization (strong overlap at -7.6 eV) contributes to the improved adsorption energy in Si-doped MgO. Ti doping exhibits the most pronounced electronic interactions. A dominant Ti peak appears at -0.2 eV, overlapping with the major O peak of CO<sub>2</sub>. This indicates strong orbital hybridization and the formation of a new Mg-O bond, which stabilizes the adsorbed CO<sub>2</sub> molecule. An additional overlap occurs at -0.6 eV, where the O peak of CO<sub>2</sub> interacts with the Mg peak, further enhancing stability. Therefore, the strong Ti-O hybridization, characterized by the overlap at -0.2 eV, along with the formation of new Mg-O bonds, as revealed by the DOS analysis, leads to the exceptional adsorption energy observed for Ti-doped MgO. This substantial electron polarization and bond formation make Ti-doped MgO the most effective surface for CO<sub>2</sub> adsorption.



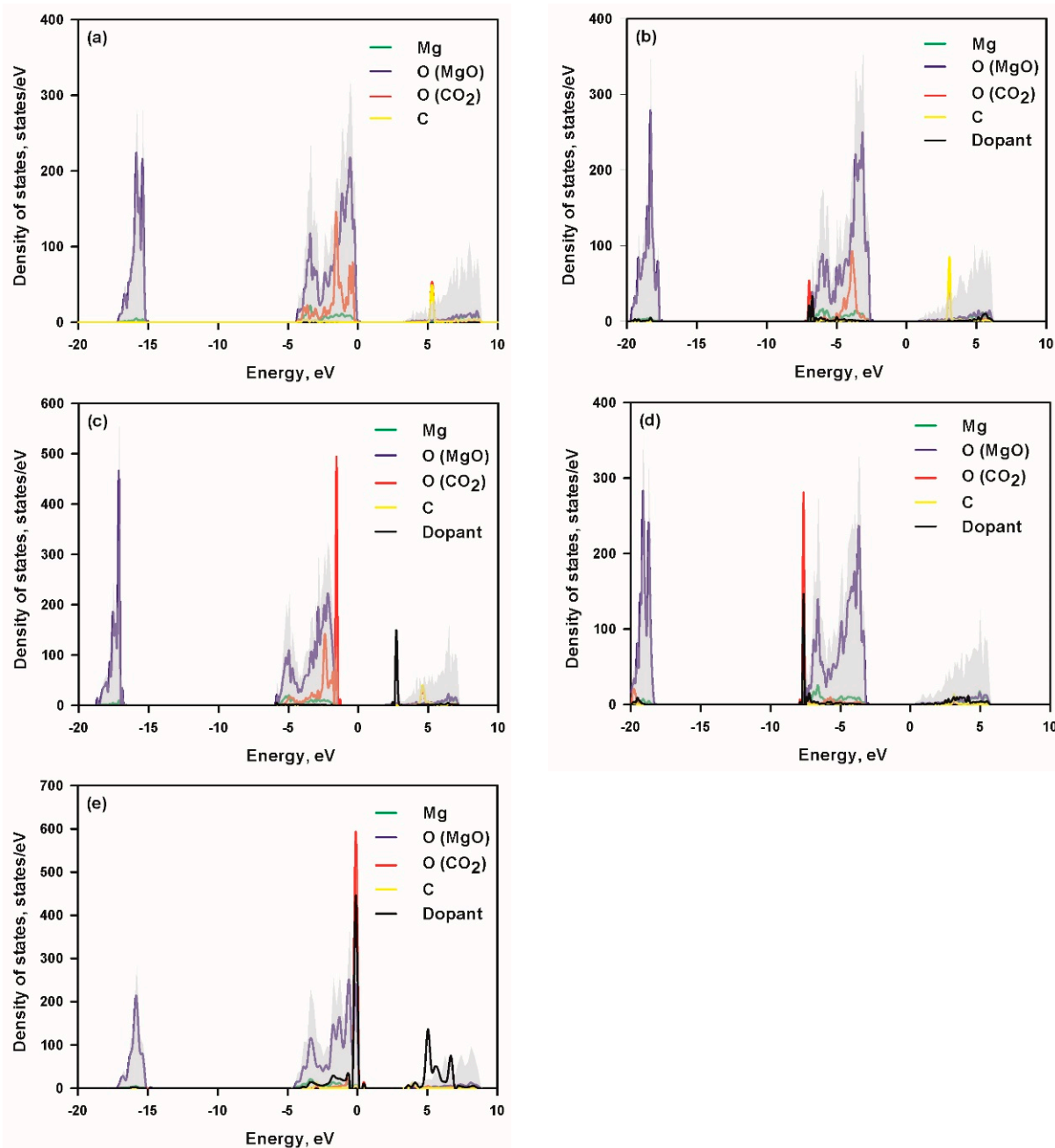


**Figure 2.** Total and projected density of states of MgO (a) and MgO doped with Al (b), C (c), Si (d), and Ti (e) after CO<sub>2</sub> adsorption. O (MgO) and O (CO<sub>2</sub>) denote O from MgO and O from CO<sub>2</sub>, respectively.

The charge transfer capacity of each dopant compared with that of Mg in pristine MgO is presented in Table 4. To understand the gain and loss of electrons in the adsorbed CO<sub>2</sub> molecules, the net charges of CO<sub>2</sub> and its two components, O<sub>1</sub> and O<sub>2</sub>, are also summarized in Table 4. The minus sign indicates the acceptance of electrons. In pristine MgO, the charge transfer from the surface to the CO<sub>2</sub> molecule is relatively weak. The CO<sub>2</sub> molecule accepts a moderate total charge of  $-0.50 e^-$ , distributed equally across the two O atoms ( $-0.63 e^-$  for O<sub>1</sub> and O<sub>2</sub>). This symmetric charge distribution indicates a weak physisorption mechanism, where no significant electron redistribution occurs to destabilize the CO<sub>2</sub> molecule. The Al in Al-doped MgO introduces a noticeable increase in the charge transfer capacity compared with pristine MgO. CO<sub>2</sub> accepts  $-0.71 e^-$  overall, which is higher than pristine MgO. However, the charge distribution across the two O atoms remains symmetric

(O<sub>1</sub>:  $-0.65 e^-$  and O<sub>2</sub>:  $-0.68 e^-$ ). The symmetric electron distribution indicates that no significant polarization occurs in the CO<sub>2</sub> molecule. C-doped MgO exhibits the highest charge transfer capacity among the dopants, substantially increasing the electron density on the MgO surface. Although CO<sub>2</sub> does not accept significantly more electrons compared with pristine MgO, the electrons donated by C are redistributed to surface atoms, increasing the surface basicity (more O<sup>2-</sup> sites) and enhancing the interaction with CO<sub>2</sub>. Moreover, the slight charge asymmetry in O<sub>1</sub> and O<sub>2</sub> reflects minor polarization of the CO<sub>2</sub> molecule, contributing to moderate CO<sub>2</sub> stabilization. Si contributes significant charge transfer to the surface, surpassing Al but falling below C. CO<sub>2</sub> accepts  $-1.18 e^-$ , which is the highest among all dopants; however, the charge distribution is slightly asymmetric (O<sub>1</sub>:  $-0.59 e^-$  and O<sub>2</sub>:  $-0.60 e^-$ ). Ti provides substantial charge transfer to the MgO surface, although lower than C or Si. CO<sub>2</sub> accepts  $-0.91 e^-$  overall. However, the charge distribution is highly asymmetric (O<sub>1</sub>:  $-0.20 e^-$  and O<sub>2</sub>:  $-0.88 e^-$ ). The uneven electron distribution between O<sub>1</sub> and O<sub>2</sub> (charge difference of  $0.68 e^-$ ) strongly polarizes the CO<sub>2</sub> molecule. This polarization induces partial breakage of the CO<sub>2</sub> bond, leading to a chemically activated state and the formation of new Mg–O bonds. The strong interaction between Ti and CO<sub>2</sub> is further evidenced by DOS analysis, where strong Ti–O hybridization and new Mg–O bonds contribute to the exceptional adsorption energy. Ti doping achieves the highest CO<sub>2</sub> adsorption energy due to strong hybridization, significant charge transfer, and pronounced CO<sub>2</sub> polarization. It is observed that the degree of polarization (difference between O<sub>1</sub> and O<sub>2</sub> charges) correlates directly with adsorption energy. Ti-doped MgO exhibits the highest charge difference ( $0.68 e^-$ ) and adsorption energy. Our results also show that donation electrons to the MgO surface to increase surface basic O<sup>2-</sup> sites is beneficial to promote CO<sub>2</sub> adsorption. This analysis aligns with previous studies (Hu et al.) that emphasize the role of dopant valence in improving CO<sub>2</sub> adsorption performance [21,22]. Our findings on Ti-doped MgO suggest that transition metal elements with high valence electrons are promising candidates for further study.

**Table 4.** Charge transfer capacity of dopant and charge acceptance of CO<sub>2</sub> molecules in CO<sub>2</sub>-adsorbed MgO.

Dopant	Charge Transfer Capacity	CO <sub>2</sub>	O <sub>1</sub>	O <sub>2</sub>
-	0.56	$-0.50$	$-0.63$	$-0.63$
Al	1.29	$-0.71$	$-0.52$	$-0.52$
C	3.79	$-0.53$	$-0.65$	$-0.68$
Si	2.37	$-1.18$	$-0.59$	$-0.60$
Ti	2.00	$-0.91$	$-0.20$	$-0.88$

### 3.4. Characterization of Pristine and C-Doped MgO

Figure 3 presents scanning electron microscopy (SEM) images of pristine and C-doped MgO nanoparticles, both of which show a spherical morphology. The pristine MgO nanoparticles displayed uniformity, with an average size of around 100 nm, whereas C-doped MgO nanoparticles exhibited a broader size distribution, ranging from around 50 nm to 1  $\mu\text{m}$ . Our observations are in line with previous studies, which reported changes in particle size distribution in carbon-doped materials compared with their pristine counterparts [46,47].

The structural analysis of the MgO and C-MgO were carried out by XRD analysis. Figure 4 presents the XRD spectra of the two samples, showing 2 $\theta$  peaks at  $36.7^\circ$ ,  $42.6^\circ$ ,  $62.0^\circ$ ,  $74.2^\circ$ , and  $78.2^\circ$ , corresponding to the (111), (200), (220), (311), and (222) lattice planes, respectively. These peaks are consistent with the standard MgO pattern (ICDD 00-045-0946). We highlight that our theoretical calculations employed identical lattice parameters for all structures, both pristine and doped. This approach is validated by the XRD spectra,

which demonstrate consistent lattice parameters and structural symmetry for C-doped MgO compared with pristine MgO. Moreover, the broader full width at half maximum (FWHM) observed in the XRD peaks for C-doped MgO supports our conclusion that C doping introduces defects. These defects arise from the displacement of the doped C atom from its original Mg lattice site, as shown in Figure 2c. The carbon content in the C-doped MgO sample was determined using CHNS analysis and measured to be 5.07%.

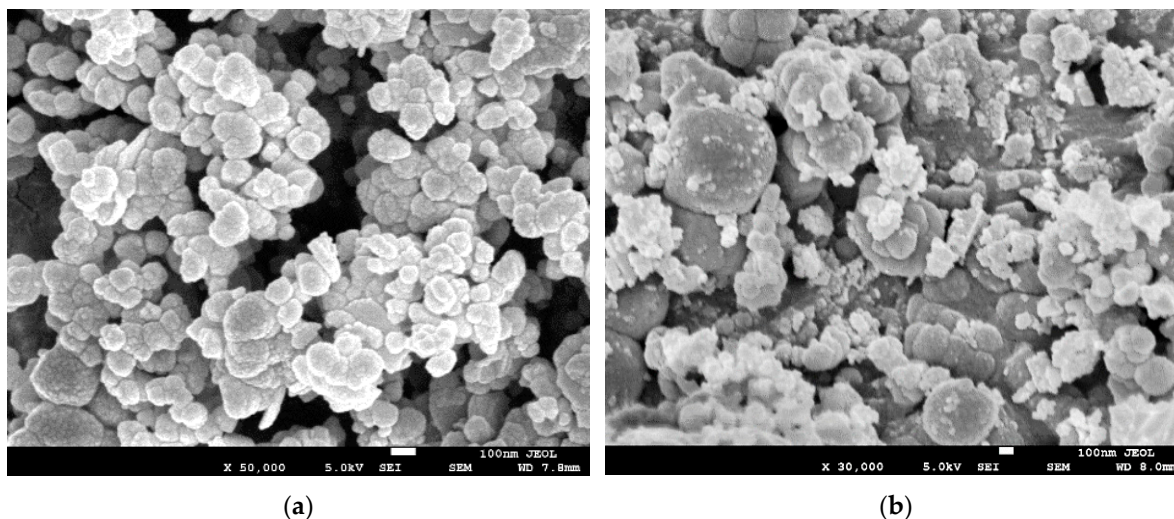


Figure 3. SEM images of spray-dried pristine MgO nanoparticles (a) and C-doped MgO nanoparticles (b).

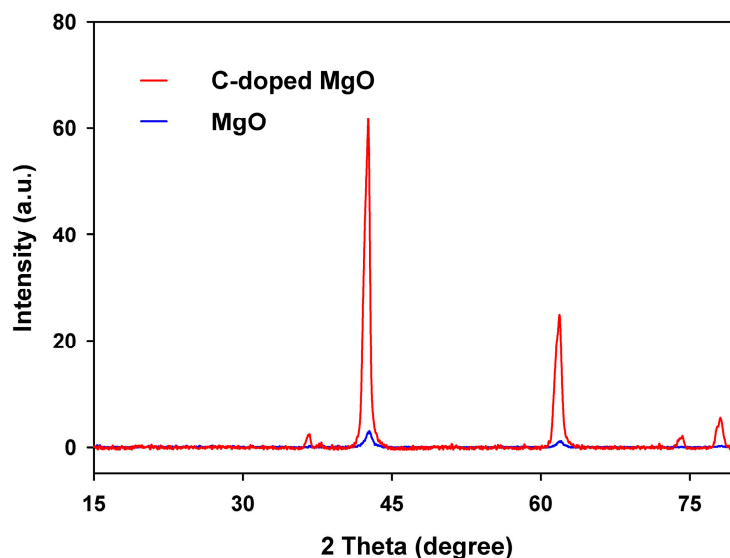


Figure 4. XRD spectra of MgO and C-doped MgO nanoparticles.

### 3.5. Measured CO<sub>2</sub> Adsorption on Pristine and C-Doped MgO

The CO<sub>2</sub> adsorption capacity was determined using thermogravimetric analysis. The increase in sample weight, i.e., the adsorbed CO<sub>2</sub> amount, is recorded over time under a CO<sub>2</sub> gas feed, as depicted in Figure 5 for pristine and C-doped MgO, respectively. It is evident that carbon doping has significantly increased CO<sub>2</sub> adsorption, effectively doubling it compared with pristine MgO. Specifically, the CO<sub>2</sub> capacity of the pristine MgO sample is 22.7 mg/g, whereas the C-doped MgO sample exhibits a remarkable capacity of 45.0 mg/g. The C-doped MgO shows higher CO<sub>2</sub> adsorption capacity compared with the reported values of MgO doped with Zn (33.3 mg/g) [4], Al (34.1 mg/g) [12], and Cu (34.6 mg/g) [14].

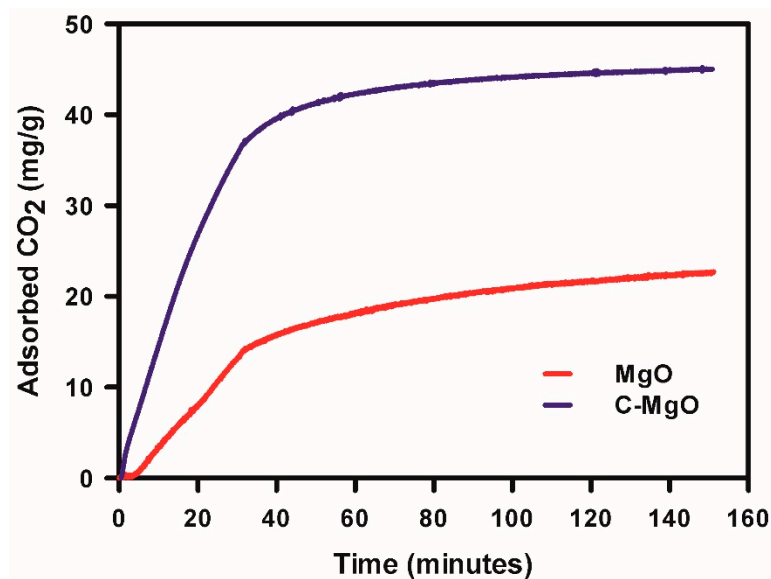


Figure 5. CO<sub>2</sub> adsorption capacity of MgO and C-doped MgO.

#### 4. Conclusions

In conclusion, while significant efforts have been dedicated to enhancing CO<sub>2</sub> adsorption in MgO through the introduction of dopants, the persistent absence of explicit dopant selection guidelines and a comprehensive understanding of the underlying mechanisms remain ongoing challenges. Our investigation employed a synergistic approach that combines first-principles calculations with experimentation to explore the structural modifications in MgO doped with high-valence elements (Al, C, Si, and Ti) and their interactions with CO<sub>2</sub>. Structural analysis revealed that the dopants induced notable changes in bond lengths and surface geometry, particularly with Ti and C showing significant displacements. The doping formation energy indicated that Al doping is thermodynamically more favorable, while C doping is the toughest due to its higher energy requirement. CO<sub>2</sub> adsorption studies demonstrated that all dopants enhanced the CO<sub>2</sub> adsorption energy compared with pristine MgO, with Ti and C doping exhibiting the most pronounced improvements. Our findings uncovered two distinct mechanisms that govern CO<sub>2</sub> capture: Ti-induced catalytic CO<sub>2</sub> decomposition and CO<sub>2</sub> polarization driven by Al, C, and Si. Specifically, Ti doping prompted structural distortion and outward displacement of Ti atoms, facilitating CO<sub>2</sub> dissociation, while C doping significantly increased the electron donation capacity and CO<sub>2</sub> adsorption energy. In the case of pristine and C-doped MgO, CO<sub>2</sub> engagement predominantly occurred through interactions with surface O atoms, whereas Al-, Si-, and Ti-doped MgO relied primarily on interactions between the dopant and O atoms.

Experimental validation through CO<sub>2</sub> adsorption measurements confirmed the superior performance of C-doped MgO, achieving a remarkable CO<sub>2</sub> uptake of 45.0 mg/g—double that of pristine MgO and surpassing previously reported doped systems. This enhanced adsorption can be attributed to the increased charge donation capacity and surface basicity introduced by C doping, which facilitate stronger CO<sub>2</sub> interactions.

Overall, our findings demonstrate that selective doping of MgO with high-charge-transfer elements such as C and Ti effectively enhances CO<sub>2</sub> adsorption performance. These results provide profound insights into the mechanisms and principles for dopant selection and design. Future studies should explore the role of transition metal dopants and their potential for synergistic effects in CO<sub>2</sub> capture and conversion technologies.

**Supplementary Materials:** The following supporting information can be downloaded at: <https://www.mdpi.com/article/10.3390/biomimetics10010009/s1>, Figure S1: Typical adsorption sites of doped MgO; Table S1: Procedure for simulating CO<sub>2</sub> adsorption on doped MgO (100) surfaces.

**Author Contributions:** Conceptualization, P.W. and S.W.; methodology, S.W. and H.N.T.; validation, S.W. and H.N.T.; investigation, S.W., W.P.C.L. and H.N.T.; data curation, S.W. and H.N.T.; visualization, S.W.; writing—original draft preparation, S.W. and H.N.T.; writing—review and editing, S.W., W.P.C.L. and H.N.T.; project administration, X.L. and P.W.; funding acquisition, P.W. All authors have read and agreed to the published version of the manuscript.

**Funding:** This research was funded by MOE2018-T2-1-163 of the Ministry of Education, Singapore; AME Individual Research Grant (A20E7c0108) of the Agency for Science, Technology and Research, Singapore; the Marine Science Research and Development program (MSRDP-P28) of the National Research Foundation, Prime Minister's Office, Singapore; the MOE-T1-program (SKI 2021\_02\_15) of the Ministry of Education, Singapore.

**Institutional Review Board Statement:** Not applicable.

**Informed Consent Statement:** Not applicable.

**Data Availability Statement:** The data presented in this study are available upon request from the corresponding author.

**Acknowledgments:** The first-principles calculations were conducted using the resources of the National Supercomputing Centre, Singapore.

**Conflicts of Interest:** The authors declare no conflicts of interest.

## References

1. IPCC. Climate Change 2021: The Physical Science Basis. In *Contribution of Working Group I to the Sixth Assessment Report of the Intergovernmental Panel on Climate Change*; Masson-Delmotte, V., Zhai, P., Pirani, A., Connors, S.L., Péan, C., Berger, S., Caud, N., Chen, Y., Goldfarb, L., Gomis, M.I., et al., Eds.; Cambridge University Press: Cambridge, UK, 2021; p. 2391.
2. Zeng, H.; Qu, X.; Xu, D.; Luo, Y. Porous Adsorption Materials for Carbon Dioxide Capture in Industrial Flue Gas. *Front. Chem.* **2022**, *10*, 939701. [[CrossRef](#)]
3. Zhu, Z.; Shi, X.; Rao, Y.; Huang, Y. Recent progress of MgO-based materials in CO<sub>2</sub> adsorption and conversion: Modification methods, reaction condition, and CO<sub>2</sub> hydrogenation. *Chin. Chem. Lett.* **2024**, *35*, 108954. [[CrossRef](#)]
4. Li, Y.Y.; Wan, M.M.; Sun, X.D.; Zhou, J.; Wang, Y.; Zhu, J.H. Novel fabrication of an efficient solid base: Carbon-doped MgO-ZnO composite and its CO<sub>2</sub> capture at 473 K. *J. Mater. Chem. A* **2015**, *3*, 18535–18545. [[CrossRef](#)]
5. Song, G.; Ding, Y.D.; Zhu, X.; Liao, Q. Carbon dioxide adsorption characteristics of synthesized MgO with various porous structures achieved by varying calcination temperature. *Colloids Surf. A-Physicochem. Eng. Asp.* **2015**, *470*, 39–45. [[CrossRef](#)]
6. Parker, A.R.; Lawrence, C.R. Water capture by a desert beetle. *Nature* **2001**, *414*, 33–34. [[CrossRef](#)]
7. Senevirathna, H.L.; Wu, S.; Lee, W.P.C.; Wu, P. Morphology Design and Fabrication of Bio-Inspired Nano-MgO-Mg(OH)<sub>2</sub> via Vapor Steaming to Enable Bulk CO<sub>2</sub> Diffusion and Capture. *Materials* **2022**, *15*, 680. [[CrossRef](#)] [[PubMed](#)]
8. Sun, Y.; Zhang, J.P.; Wen, C.; Li, Z.H. Clean production of porous MgO by thermal decomposition of Mg(OH)<sub>2</sub> using fluidized bed: Optimization for CO<sub>2</sub> adsorption. *J. Taiwan Inst. Chem. Eng.* **2016**, *63*, 170–179. [[CrossRef](#)]
9. Guo, X.; Ding, J.; Wu, Y.; Zhang, J.; Guo, G. Feasible fabrication of highly dispersed La<sub>2</sub>O<sub>3</sub> promoted MgO composites for CO<sub>2</sub> capture at mid-temperature. *Mater. Chem. Phys.* **2022**, *279*, 125734. [[CrossRef](#)]
10. Liu, M.Y.; Vogt, C.; Chaffee, A.L.; Chang, S.L.Y. Nanoscale Structural Investigation of Cs<sub>2</sub>CO<sub>3</sub>-Doped MgO Sorbent for CO<sub>2</sub> Capture at Moderate Temperature. *J. Phys. Chem. C* **2013**, *117*, 17514–17520. [[CrossRef](#)]
11. Elvira, G.B.; Francisco, G.C.; Victor, S.M.; Alberto, M.L.R. MgO-based adsorbents for CO<sub>2</sub> adsorption: Influence of structural and textural properties on the CO<sub>2</sub> adsorption performance. *J. Environ. Sci.* **2017**, *57*, 418–428. [[CrossRef](#)]
12. Niu, X.D.; Feng, Y.Y.; Xu, Y.H.; Yang, W. Synthesis of hollow Al-doped MgO spheres via a sacrificial templating method for enhanced CO<sub>2</sub> adsorption. *J. Nat. Gas Sci. Eng.* **2021**, *88*, 10. [[CrossRef](#)]
13. Hiremath, V.; Trivino, M.L.T.; Shavi, R.; Gebresillase, M.N.; Seo, J.G. Sacrificial templating method for fabrication of MgO-Al<sub>2</sub>O<sub>3</sub>@C spheres and their application to CO<sub>2</sub> capture. *Mater. Lett.* **2018**, *211*, 304–307. [[CrossRef](#)]
14. Li, Y.Y.; Dong, X.Y.M.; Sun, X.D.; Wang, Y.; Zhu, J.H. New Solid-Base Cu-MgO for CO<sub>2</sub> Capture at 473 K and Removal of Nitrosamine. *Acs Appl. Mater. Interfaces* **2016**, *8*, 30193–30204. [[CrossRef](#)]

15. Jiao, X.; Li, L.; Li, H.G.; Xiao, F.K.; Zhao, N.; Wei, W.; Zhang, B.S. Influence of preparation parameters on the structural properties and the CO<sub>2</sub> capture performance of Mg-Zr solid sorbent. *Mater. Res. Bull.* **2015**, *64*, 163–170. [CrossRef]
16. Kwak, J.S.; Kim, K.Y.; Oh, K.R.; Kwon, Y.U. Performance enhancement of all-solid CO<sub>2</sub> absorbent based on Na<sub>2</sub>CO<sub>3</sub>-promoted MgO by using ZrO<sub>2</sub> dispersant. *Int. J. Greenh. Gas Control* **2019**, *81*, 38–43. [CrossRef]
17. Tosoni, S.; Spinnato, D.; Pacchioni, G. DFT Study of CO<sub>2</sub> Activation on Doped and Ultrathin MgO Films. *J. Phys. Chem. C* **2015**, *119*, 27594–27602. [CrossRef]
18. Hu, P.; Wang, S.; Zhuo, Y. CO<sub>2</sub> adsorption enhancement over alkaline metal-promoted MgO with SO<sub>2</sub>, O<sub>2</sub>, and H<sub>2</sub>O present: A theoretical study. *Sep. Purif. Technol.* **2022**, *284*, 120253. [CrossRef]
19. Jang, J.M.; Kang, S.G. Understanding CO<sub>2</sub> Adsorption on a M-1 (M-2)-Promoted (Doped) MgO-CaO(100) Surface (M-1 = Li, Na, K, and Rb, M-2 = Sr): A DFT Theoretical Study. *Acs Sustain. Chem. Eng.* **2019**, *7*, 16979–16984. [CrossRef]
20. Mazheika, A.; Levchenko, S.V. Ni Substitutional Defects in Bulk and at the (001) Surface of MgO from First-Principles Calculations. *J. Phys. Chem. C* **2016**, *120*, 26934–26944. [CrossRef]
21. Hu, P.; Wang, S.; Zhuo, Y. Research on CO<sub>2</sub> adsorption performances of metal-doped (Ca, Fe and Al) MgO. *Sep. Purif. Technol.* **2021**, *276*, 119323. [CrossRef]
22. Hu, P.; Wang, S.; Zhuo, Y. Strengthened CO<sub>2</sub> adsorption over Ce/Al-promoted MgO for fast capture. *Sep. Purif. Technol.* **2022**, *287*, 120518. [CrossRef]
23. Manz, T.A.; Limas, N.G. Introducing DDEC6 atomic population analysis: Part 1. Charge partitioning theory and methodology. *Rsc Adv.* **2016**, *6*, 47771–47801. [CrossRef]
24. Limas, N.G.; Manz, T.A. Introducing DDEC6 atomic population analysis: Part 2. Computed results for a wide range of periodic and nonperiodic materials. *Rsc Adv.* **2016**, *6*, 45727–45747. [CrossRef]
25. Manz, T.A. Introducing DDEC6 atomic population analysis: Part 3. Comprehensive method to compute bond orders. *Rsc Adv.* **2017**, *7*, 45552–45581. [CrossRef]
26. Limas, N.G.; Manz, T.A. Introducing DDEC6 atomic population analysis: Part 4. Efficient parallel computation of net atomic charges, atomic spin moments, bond orders, and more. *Rsc Adv.* **2018**, *8*, 2678–2707. [CrossRef]
27. Kresse, G.; Furthmüller, J. Efficient iterative schemes for ab initio total-energy calculations using a plane-wave basis set. *Phys. Rev. B* **1996**, *54*, 11169–11186. [CrossRef]
28. Hammer, B.; Hansen, L.B.; Norskov, J.K. Improved adsorption energetics within density-functional theory using revised Perdew-Burke-Ernzerhof functionals. *Phys. Rev. B* **1999**, *59*, 7413–7421. [CrossRef]
29. Kresse, G.; Joubert, D. From ultrasoft pseudopotentials to the projector augmented-wave method. *Phys. Rev. B* **1999**, *59*, 1758–1775. [CrossRef]
30. Kresse, G.; Furthmüller, J. Efficiency of ab-initio total energy calculations for metals and semiconductors using a plane-wave basis set. *Comput. Mater. Sci.* **1996**, *6*, 15–50. [CrossRef]
31. Grimme, S.; Antony, J.; Ehrlich, S.; Krieg, H. A consistent and accurate ab initio parametrization of density functional dispersion correction (DFT-D) for the 94 elements H-Pu. *J. Chem. Phys.* **2010**, *132*, 19. [CrossRef]
32. Monkhorst, H.J.; Pack, J.D. Special points for brillouin-zone integrations. *Phys. Rev. B* **1976**, *13*, 5188–5192. [CrossRef]
33. Wu, S.; Tan, B.T.; Senevirathna, H.L.; Wu, P. Polarization of CO<sub>2</sub> for improved CO<sub>2</sub> adsorption by MgO and Mg(OH)<sub>2</sub>. *Appl. Surf. Sci.* **2021**, *562*, 150187. [CrossRef]
34. Hayun, S.; Tran, T.; Ushakov, S.V.; Thron, A.M.; van Benthem, K.; Navrotsky, A.; Castro, R.H.R. Experimental Methodologies for Assessing the Surface Energy of Highly Hygroscopic Materials: The Case of Nanocrystalline Magnesia. *J. Phys. Chem. C* **2011**, *115*, 23929–23935. [CrossRef]
35. Chargemol. Available online: <http://sourceforge.net/projects/ddec/> (accessed on 21 July 2021).
36. Rumble, J. (Ed.) *CRC Handbook of Chemistry and Physics*, 102 ed.; CRC Press: Boca Raton, FL, USA, 2021.
37. Jain, A.; Ong, S.P.; Hautier, G.; Chen, W.; Richards, W.D.; Dacek, S.; Cholia, S.; Gunter, D.; Skinner, D.; Ceder, G.; et al. Commentary: The Materials Project: A materials genome approach to accelerating materials innovation. *APL Mater.* **2013**, *1*, 011002. [CrossRef]
38. Niedermaier, M.; Schwab, T.; Dolcetti, P.; Bernardi, J.; Gross, S.; Bockstedte, M.; Diwald, O. Cobalt and Iron Ions in MgO Nanocrystals: Should They Stay or Should They Go. *J. Phys. Chem. C* **2019**, *123*, 25991–26004. [CrossRef]
39. Hao, X.; Wang, B.; Wang, Q.; Zhang, R.; Li, D. Insight into both coverage and surface structure dependent CO adsorption and activation on different Ni surfaces from DFT and atomistic thermodynamics. *Phys. Chem. Chem. Phys.* **2016**, *18*, 17606–17618. [CrossRef]
40. Ranjan, P.; Saptal, V.B.; Bera, J.K. Recent Advances in Carbon Dioxide Adsorption, Activation and Hydrogenation to Methanol using Transition Metal Carbides. *ChemSusChem* **2022**, *15*, e202201183. [CrossRef] [PubMed]
41. Kim, K.; Han, J.W.; Lee, K.S.; Lee, W.B. Promoting alkali and alkaline-earth metals on MgO for enhancing CO<sub>2</sub> capture by first-principles calculations. *Phys. Chem. Chem. Phys.* **2014**, *16*, 24818–24823. [CrossRef]
42. Lv, G.; Zhu, C.; Zhang, H.; Su, Y.; Qian, P. Mechanism of CO<sub>2</sub> adsorption on point-defective MgO surfaces: First-principles study. *Appl. Surf. Sci.* **2022**, *604*, 154647. [CrossRef]

43. Pan, Y.-X.; Liu, C.-J.; Wiltowski, T.S.; Ge, Q. CO<sub>2</sub> adsorption and activation over  $\gamma$ -Al<sub>2</sub>O<sub>3</sub>-supported transition metal dimers: A density functional study. *Catal. Today* **2009**, *147*, 68–76. [[CrossRef](#)]
44. Do, H.; Truong, H.B. Ni, Co, Zn, and Cu metal-organic framework-based nanomaterials for electrochemical reduction of CO<sub>2</sub>: A review. *Beilstein J. Nanotechnol.* **2023**, *14*, 904–911. [[CrossRef](#)]
45. Wang, L.; Hou, T.; Li, Y.; Lu, H.; Gao, L. Lubrication Performances of Carbon-Doped MoSe<sub>2</sub> Nanoparticles and Their Biocompatibility Characterization In Vitro. *Front. Chem.* **2021**, *8*, 580151. [[CrossRef](#)] [[PubMed](#)]
46. Jerin, I.; Rahman, M.A.; Khan, A.H.; Hossain, M.M. Photocatalytic degradation of methylene blue under visible light using carbon-doped titanium dioxide as photocatalyst. *Desalination Water Treat.* **2024**, *320*, 100711. [[CrossRef](#)]
47. Hafner, J. Ab-initio simulations of materials using VASP: Density-functional theory and beyond. *J. Comput. Chem.* **2008**, *29*, 2044–2078. [[CrossRef](#)]

**Disclaimer/Publisher’s Note:** The statements, opinions and data contained in all publications are solely those of the individual author(s) and contributor(s) and not of MDPI and/or the editor(s). MDPI and/or the editor(s) disclaim responsibility for any injury to people or property resulting from any ideas, methods, instructions or products referred to in the content.